PHYSICAL SCIENCES

# High–spatiotemporal resolution deuterium metabolic imaging enables in vivo phenotyping of intra- and intertumoral heterogeneity

**Xinjie Liu[1,2]†, Sufei Wang[3]†, Jinrui Zhao[1], ShaSha Wang[1], Peng Sun[4], Xin Zhou[1,2], Maili Liu[1,2], Chaoyang Liu[1,2], Lucio Frydman[5]*, Qingjia Bao[1,2]***



**Intra- and intertumoral heterogeneities raise fundamental biological questions and have important implications for accurate cancer diagnosis, prognosis, and treatment. These heterogeneities reflect tumor complexity, including a pronounced diversity in metabolic phenotypes and profiles. This study demonstrates that in vivo deuterium metabolic imaging (DMI) data acquired with sufficiently high spatiotemporal resolution provide a minimally invasive approach to assess these heterogeneities. A multifrequency DMI approach was used to examine tumor heterogeneities within and between colon cancer models. Regions of high and low glucose enrichment and labeled lactate accumulation could thus be detected; these were analyzed using unsupervised clustering strategies based on *k*-means clustering of area-under-the-curve information, and principal components analysis with Gaussian mixture modeling. Spatial alignment of these imaging-derived clusters for $^{2}$H-glucose and $^{2}$H-lactate showed good agreement with each other as well as with histological sections, validating the biological relevance of the identified subregions. Immunohistochemical analyses showed that glucose-enriched subregions were positively correlated with the expression of GLUT1 and DLAT, while lactate-enriched areas showed elevated expression of LDHA and MCT4. These results demonstrate that in vivo DMI can distinguish metabolically distinct subregions within viable tumors and between tumor models. DMI-based metabolic maps could thus provide the means to characterize intra- and intertumoral heterogeneities, paving the way for imaging-based metabolic phenotyping in precision oncology.**

## INTRODUCTION

Intratumoral heterogeneity—the coexistence of distinct tissue subtypes within a tumor—is a defining feature of cancer, closely linked to disease progression, therapeutic resistance, and relapse (*1*–*3*). Accurate intra- and intertumoral diagnoses are essential for stratifying risk and tailoring treatment, particularly to identify aggressive subclones that may evade therapy or drive metastasis (*4*–*7*). While tissue biopsies enable molecular profiling, their spatial limitations and procedural constraints restrict comprehensiveness, evaluation, and longitudinal monitoring (*8*, *9*). Only minimally invasive in vivo images targeting the whole tumor can provide the assessments and repeated measurements needed for a full characterization and understanding of the disease and its development (*10*, *11*). Routine imaging modalities, however, provide mostly morphological descriptors that lack sufficient spatially resolved metabolic insight, underscoring the need for discovering previously unrecognized functional and molecular biomarkers (*12*, *13*). The present study discusses the opportunities that novel forms of deuterium metabolic imaging (DMI) having high sensitivity and improved spatiotemporal resolution provide in this realm.

One of the main sources of insight about metabolic reprogramming is the Warburg effect, a hallmark of cancer and a common imaging target (*14*, *15*). Clinically approved [$^{18}$F]fluorodeoxyglucose positron emission tomography (FDG-PET) relies on this effect to quantify glucose enrichment (*16*), revealing within the limits of its spatial resolution variations in tumor metabolism, yet lacking the specificity needed for discerning downstream pathways (*17*, *18*). Conventional $^{1}$H magnetic resonance imaging (MRI) provides, primarily, anatomical and physiological contrasts that do not directly report pathway-specific metabolism (*19*, *20*). By contrast, diffusion and perfusion MRI have demonstrated pronounced intratumoral heterogeneities, related to cellularity and vascular supply (*3*). Metabolic specificity can be introduced by $^{1}$H magnetic resonance spectroscopic imaging (MRSI) and related techniques such as chemical exchange saturation transfer and hyperpolarized $^{13}$C MRSI (*21*–*27*). However, robust mapping of metabolic heterogeneity by these means is often limited in practice by spatial resolution, coverage, temporal sampling, sensitivity, and quantification constraints.

Recently, DMI has emerged as a promising technique for noninvasively assessing tissue metabolic kinetics without some of these constraints (*18*–*20*, *28*). DMI follows the fate of deuterated, nonradioactive substrates (*29*). $^{2}$H-labeled metabolites minimally perturb the endogenous metabolic pathways, enabling the continuous monitoring of substrate enrichment and downstream metabolic conversions under physiological conditions (*30*–*32*). In addition, the relatively short $T_1$ relaxation time of $^{2}$H compared to $^{13}$C facilitates signal averaging across multiple acquisitions, improving the signal-to-noise ratio (SNR) within clinically feasible scan durations (*33*, *34*). Numerous studies have demonstrated the potential of DMI in oncological applications, including tumor detection, molecular subtype classification, and early therapeutic response assessment (*20*, *31*, *32*, *35*–*40*). For instance, DMI has been used to differentiate tumor phenotypes based on their glucose metabolism pathways, and to identify treatment-induced reductions in lactate accumulation following chemotherapy

[1]State Key Laboratory of Magnetic Resonance Spectroscopy and Imaging, Innovation Academy for Precision Measurement Science and Technology, Chinese Academy of Sciences, Wuhan 430071, China. [2]University of Chinese Academy of Sciences, Beijing 100049, China. [3]Department of Respiratory and Critical Care Medicine, Union Hospital, Tongji Medical College, Huazhong University of Science and Technology, Wuhan 430022, China. [4]Neusoft Medical Systems Co. Ltd., Shenyang 110167, China. [5]Weizmann Institute of Science, 7600100 Rehovot, Israel.
*Corresponding author. Email: lucio.frydman@weizmann.ac.il (L.F.); qingjia.bao@apm.ac.cn (Q.B.)
†These authors contributed equally to this work.

or targeted therapy (*19*, *38*–*40*). In vivo DMI technologies could also provide valuable insight into intratumoral metabolic heterogeneity, provided its relatively low spatiotemporal resolution can be overcome (*18*, *19*). This is challenged by $^{2}$H's limited sensitivity and by low metabolic concentrations, which together impair DMI's ability to spatially resolve intratumoral heterogeneities and metabolic fluxes at the microliter level. Being able to access such localized metabolic kinetics could be essential for accurate diagnosis, subtype stratification, and personalized treatment planning, as well as for a better understanding of cancer.

This study presents a high-resolution DMI strategy that, when integrated with unsupervised clustering, enables such mapping of intratumoral metabolic heterogeneity in vivo (Fig. 1). It also enables the discrimination among different tumor subtypes. To achieve such goals, we rely on a multifrequency version of the balanced steady-state free precession (bSSFP) DMI pulse sequence that leverages the distinct spectral responses of the different metabolites. At 9.4-T fields, this provided a robust spectral separation of the multiple deuterated species arising following [6,6′-$^{2}$H$_2$]glucose administration, while achieving submillimeter (0.9 mm × 0.9 mm) in-plane resolution at ~2 min per dynamic frame. The metabolic heterogeneity data that these fast, high-resolution DMI experiments provided were analyzed by two complementary, unsupervised clustering pipelines: one involving *k*-means clustering of area-under-the-curve (AUC) data,

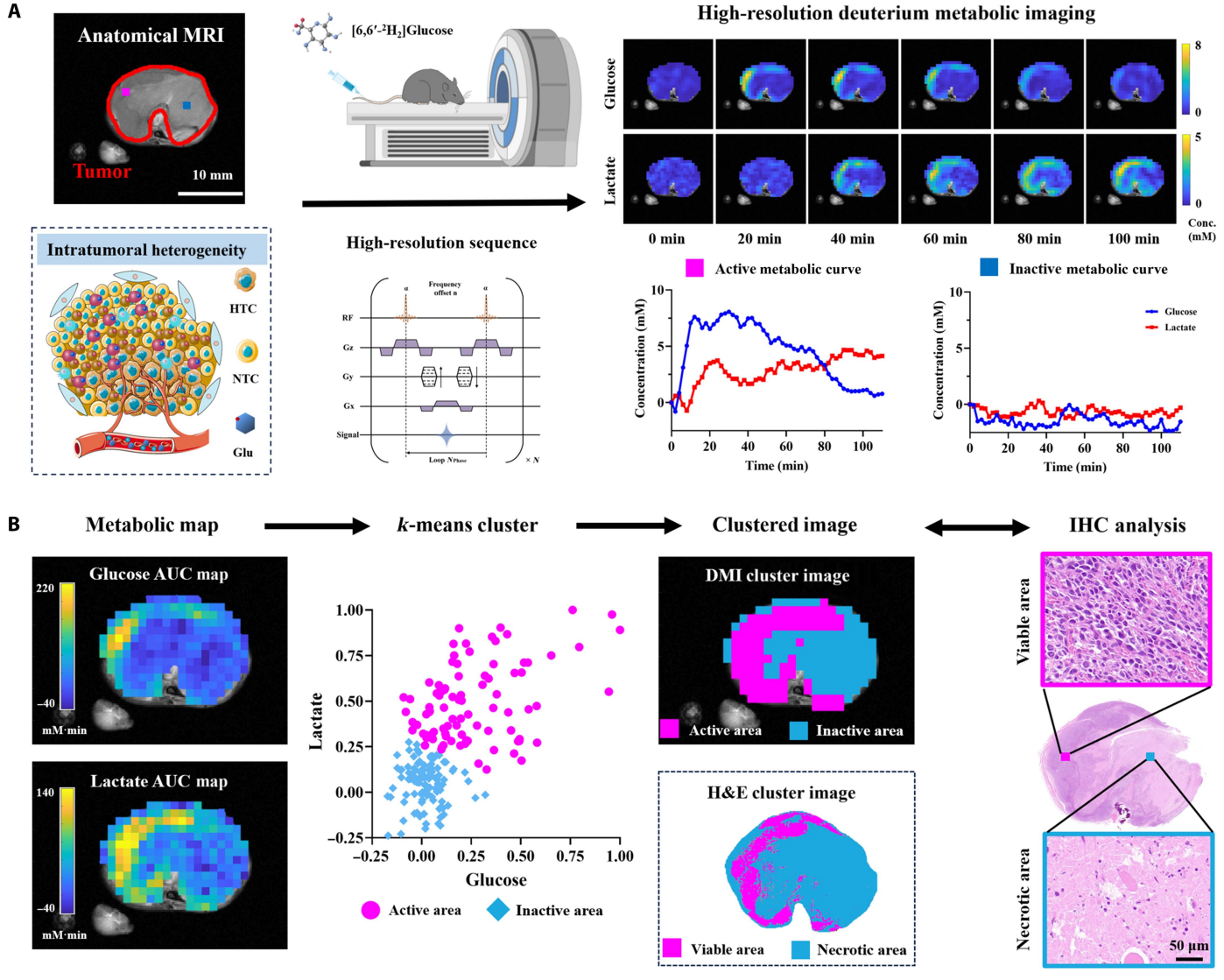


**Fig. 1. Integrated DMI and computational framework used for the in vivo mapping of metabolic tumor heterogeneities.** (**A**) After intravenous administration of [6,6′-$^{2}$H$_2$]glucose in a CT26 tumor–bearing mice, dynamic high-resolution DMI was performed using a bSSFP-based sequence with high spatial and temporal resolution. This enabled voxel-wise mapping of glucose enrichment and lactate accumulation over time, revealing distinct tumor subregions exhibiting differential glycolytic metabolism. (**B**) Dynamic metabolic data were then processed to generate AUC maps for glucose and lactate, analyzed by *k*-means clustering strategies. The DMI clustering maps identified metabolically distinct subregions and were coregistered with H&E clustering maps, confirming that metabolically active areas corresponded to viable tumor areas, while areas with low or absent signal aligned with necrotic tissue. The viable-area and necrotic-area micrographs are magnified views of the magenta- and cyan-boxed regions, respectively, in the whole-section histology image.

the other involving a principal components analysis (PCA) followed by Gaussian mixture modeling (GMM). This integrated framework provided us with three capabilities that we believe are key for cancer understanding and diagnosis: (i) the noninvasive detection of early tumor apoptosis through reduced glycolytic flux and altered metabolite distributions, offering a sensitive MRI biomarker for detecting necrotic tumor areas as induced by excessive proliferation or by therapy; (ii) a clear picture of intratumoral metabolic heterogeneities within viable growing tumors, delineating subregions associated with distinct states such as high glucose enrichment and high lactate accumulation; and (iii) metabolic fingerprints derived from different tumor subregions, enabling the differentiation between two colorectal tumor models (intertumor heterogeneity) in a label-free, purely data-driven manner. The meaning of these in vivo heterogeneity mapping was further examined by immunohistochemical studies focusing on eight key metabolism-related markers, which confirmed and provided further insight into the functional meaningfulness of the DMI metabolic information. Collectively, these results establish high-resolution DMI with unsupervised clustering as a robust platform for metabolic phenotyping, endowed with a strong translational potential for diagnosis, treatment response evaluation, and therapeutic stratification.

## RESULTS

### High-resolution DMI enabled by multifrequency bSSFP

To enhance DMI's spatiotemporal resolution sufficiently to characterize metabolic tumor heterogeneities, it is necessary to increase its sensitivity per unit time. To this end, we relied on bSSFP experiments that have been demonstrated to provide a superior DMI sensitivity and modified them into a multifrequency (MF) bSSFP version (Fig. 2A) capable of separating the three main $^2$H signals arising in this experiment: water, glucose, and lactate. Like its chemical shift imaging (CSI) or multiecho (ME) bSSFP counterparts, MF-bSSFP leverages the favorable $T_2/T_1$ ratios of deuterated metabolites and the intrinsic spectral sparsity of DMI to enhance the SNR. MF-bSSFP, however, replaces the spectral evolution exploited by ME- and CSI-bSSFP, with imaging-oriented acquisitions carried out at a series of optimized, predefined offsets (Fig. 2A, left). As each metabolite's bSSFP image will have a different phase for each offset, suitable linear combinations of these variable-frequency acquisitions can separate their individual images. To maximize SNR and spectral separability, it is necessary to optimize the experimental acquisition parameters—foremost the repetition time (TR), flip angle, and frequency offsets defining the overall phase of each metabolite's images; this was done based on the a priori known chemical shifts of the metabolites (fig. S1). The resulting search yielded acquisition parameters for five offsets with characteristic magnitude and phase response profiles (Fig. 2A, center), from which an iterative reconstruction based on linear combinations could successfully resolve the spatial distributions for each metabolite, while factoring in $B_0$ field heterogeneities and $T_2$ effects.

Experimental results obtained with such a scheme were further validated with a three-dimensional (3D)–printed phantom containing three letters shaped as "A," "P," and "M," filled with $^2H_2O$ (40 mM), [6,6′-$^2H_2$]glucose (20 mM), and [3,3,3-$^2H_3$]-lactate (20 mM) respectively (Fig. 2B). Representative $^2$H magnitude and phase images acquired at five optimized frequency offsets (±190, ±110, and 0 Hz; fig. S2) exhibited uniform magnitude signal intensities yet distinct frequency-dependent contrasts. These unique phase signatures enabled clear metabolite differentiation and provided the basis for spectral separation in the reconstruction pipeline (Fig. 2A). To benchmark the performance of MF-bSSFP against conventional CSI, we compared spatially resolved metabolite maps at various resolutions (Fig. 2B). CSI at a 16 × 16 matrix resolution failed to capture fine phantom details, and although increasing the resolution to 32 × 32 marginally improved spatial clarity, it led to substantial SNR degradation, especially for lactate. By contrast, MF-bSSFP at 32 × 32 and 40 × 40 resolution achieved both high spatial fidelity and distinct metabolite separation, maintaining strong SNR even for low-concentration lactate for identical scanning times and spatial resolution conditions. Quantitative analyses of SNR across five repeated measurements are shown in Fig. 2C. MF-bSSFP achieved 2.8-fold, 4.1-fold, and 3.7-fold improvements over CSI for water (CSI: 20.2 ± 1.1; MF-bSSFP: 56.3 ± 1.2), glucose (CSI: 8.0 ± 0.9; MF-bSSFP: 32.4 ± 0.8), and lactate (CSI: 8.2 ± 1.0; MF-bSSFP: 30.2 ± 0.7), respectively. Moreover, the SNR of the reconstructed metabolite images closely matched the theoretical maximum obtained via direct signal averaging ($\sqrt{5}$ × mean for bSSFP images), confirming the high efficiency of the iterative reconstruction algorithm used to process the MF-bSSFP data. The robustness of the ensuing MF-bSSFP under varying noise levels and $B_0$ inhomogeneity is further demonstrated in fig. S3; comparisons with other methods are given in fig. S4.

### High-resolution DMI delineates necrotic and viable tumor compartments via unsupervised metabolic clustering

Distinguishing necrotic areas from viable tumor tissue is essential for understanding tumor progression and assessing therapeutic response. To this end, we applied the optimized DMI approach described above on mice having a subcutaneous colon cancer model, and quantified the dynamic distribution of metabolites using AUC maps for deuterated water, glucose, and lactate. The resulting spatial patterns revealed marked intratumoral metabolic heterogeneities (Fig. 3). Spatially distinct metabolic compartments could then be established via unsupervised analyses of the glucose and lactate AUC maps, using *k*-means clustering. Metabolically active areas exhibited substantial time-dependent accumulation of both glucose and lactate signals consistent with active glycolysis. By contrast, metabolically inactive areas showed markedly reduced metabolite enrichment, reflecting suppressed metabolic activity. To further validate these findings, we performed PCA on the dynamic metabolite maps, reducing the glucose and lactate time series to 10 dimensions, followed by clustering them using a GMM. The GMM-based segmentation closely matched the *k*-means results, and both of these exhibited strong correspondence with histopathological features (fig. S5). Hematoxylin and eosin (H&E) staining confirmed that DMI-defined metabolically inactive area corresponded to necrotic tissue, characterized by widespread cellular disintegration and nuclear pyknosis. By contrast, DMI-identified metabolically active area corresponded to viable tissue that showed densely packed, mitotically active tumor cells (Fig. 3). Histological matching was performed using sections (4 μm thickness) obtained near the central DMI plane (6 mm).

### High-resolution DMI reveals mesoscopic metabolic heterogeneities within viable tumors

The combination of high-resolution DMI with an unsupervised clustering algorithm also enabled us to discern heterogeneities in the metabolic activity within viable tumor compartments. Figure 4 illustrates

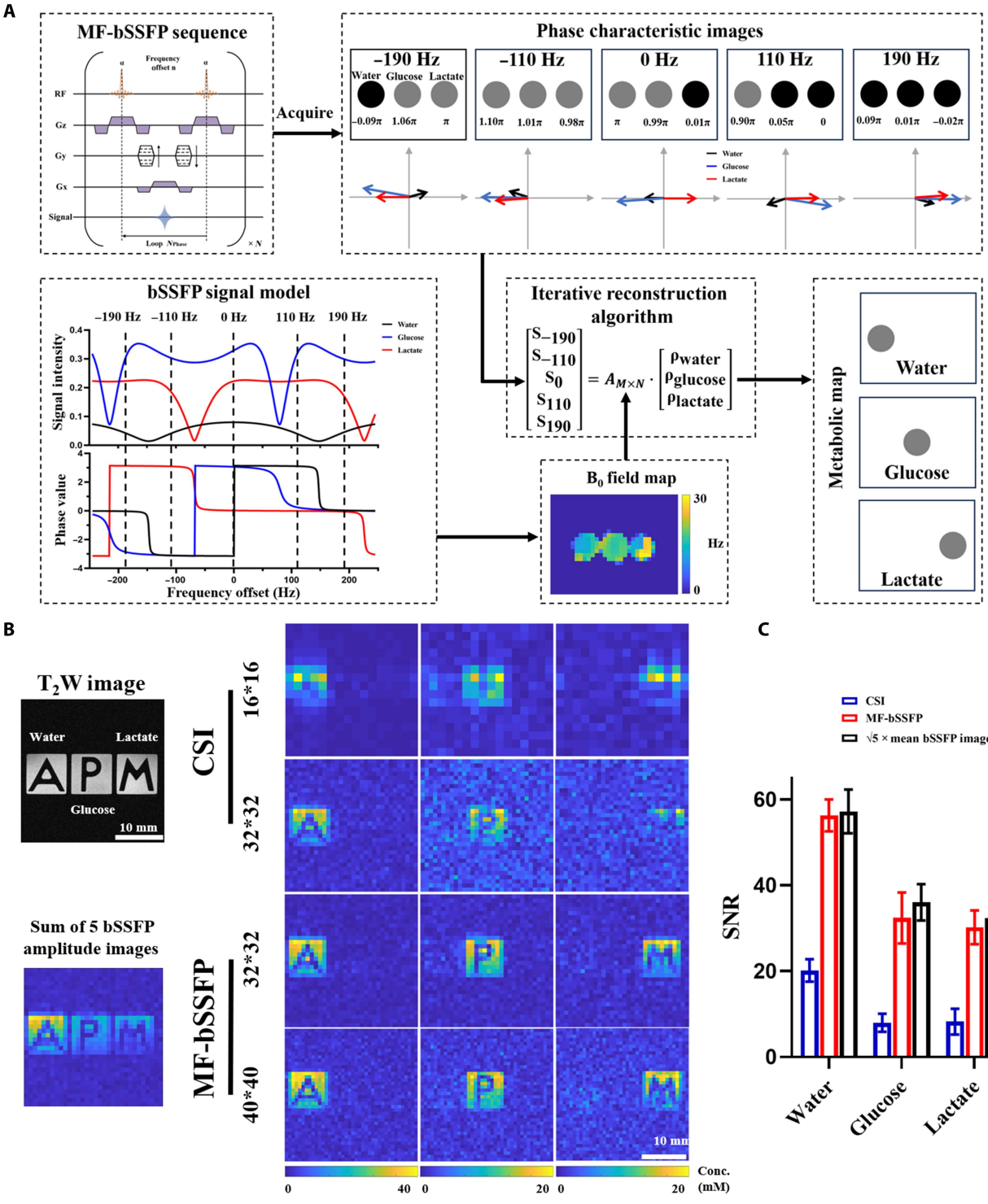


**Fig. 2. Schematic description of high spatiotemporal resolution DMI and corresponding phantom validation.** (**A**) MF-bSSFP acquisition and reconstruction pipeline, showing the sequence diagram, expected signal magnitude, and phase responses of deuterated water, glucose, and lactate across frequency offsets at 9.4 T, and the iterative reconstruction algorithm leading to metabolite-specific maps. (**B**) Left: $T_2$-weighted $^1$H image of a 3D-printed phantom containing tubes filled with $^2H_2O$ ("A"), $^2$H-glucose ("P"), and $^2$H-lactate ("M"), and sum of five $^2$H magnitude images acquired with MF-bSSFP at five frequency offsets. Right: Metabolites' maps arising from conventional CSI and MF-bSSFP acquired with same scan times (≈4 min 30 s) and field of view (30 × 30 mm$^2$). CSI was performed with matrix sizes of 16 × 16 and 32 × 32; MF-bSSFP was repeated for 32 × 32 and 40 × 40 matrices. (**C**) Quantitative SNR analysis comparing CSI and MF-bSSFP at matched resolution (32 × 32) and acquisition time. The "$\sqrt{5}$ × mean bSSFP images" bar denotes the theoretical SNR gain from combining five acquisitions. Error bars indicate SD across repeated scans (five averages each).

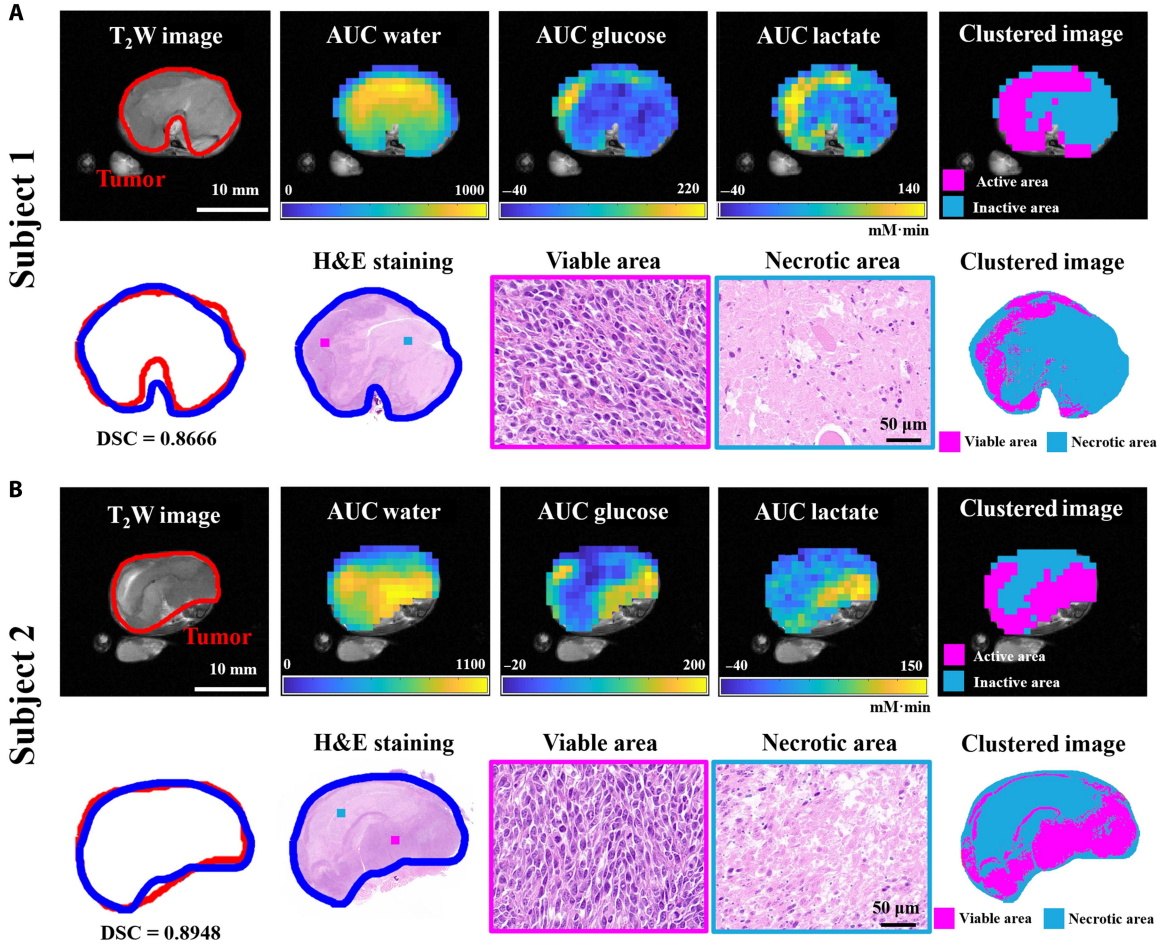


**Fig. 3. Metabolic imaging and histological validation in two tumor-bearing mice with necrotic tissue.** (**A** and **B**) $T_2$-weighted MR images with tumor boundaries (red); dynamic AUC maps of deuterated water, glucose, and lactate; DMI clustering maps; corresponding postmortem H&E sections with contours (blue); and clustered histology maps are shown for one CT26 tumor (A) and one C26 tumor (B). For subject 1, the images are the same source images as those shown in Fig. 1 and are reused here to facilitate direct comparison with the corresponding histological analysis. The viable-area and necrotic-area micrographs are magnified views of the magenta- and cyan-boxed regions, respectively, in the corresponding whole-section histology images. Clustered metabolic maps spatially matched histological features: metabolically active areas exhibited high glucose enrichment and lactate accumulation, consistent with viable area in H&E staining with dense cellularity, whereas necrotic areas showed minimal glucose enrichment and negligible lactate accumulation, aligning with necrotic areas in H&E staining with tissue disintegration and cell loss.

this with high-resolution DMI data and results arising from the unsupervised clustering, for a subcutaneous tumor mouse model. Unlike the experiments in Fig. 3, this tumor did not exhibit extensive necrosis, as confirmed by H&E staining (fig. S6). Despite the absence of large necrotic areas, DMI's high spatiotemporal resolution clearly revealed pronounced intratumoral heterogeneity, especially in the glucose enrichment and lactate accumulation (Fig. 4A). In contrast to glucose and lactate, deuterated water was not included in the present clustering analysis, as it was found to reflect a mixture of whole-body label accumulation, perfusion/vascular water content, and exchange processes, rather than a spatially specific readout of local tumor glycolytic flux at the voxel scale. There was thus little information added upon comparing results with versus without the inclusion of the AUC (water) information. (fig. S7). Therefore, *k*-means clustering applied to the glucose and lactate AUC maps identified four distinct metabolic phenotypes, with the optimal number of clusters ($K = 4$) determined using the Elbow method (Fig. 4B). The voxel-wise distribution of normalized glucose and lactate values (Fig. 4C) associated these *k*-means clustered data to one of four possible phenotypes: *HG* + *HL*: high glucose enrichment, high lactate accumulation; *HG* + *LL*: high glucose enrichment, low lactate accumulation; *LG* + *HL*: low glucose enrichment, high lactate accumulation; and *LG* + *LL*: low glucose enrichment, low lactate accumulation. These clusters appear spatially localized within the tumor (Fig. 4D).

Time-resolved glucose and lactate concentration curves for 12 C26-implanted tumor-bearing mice (Fig. 4, E and F) also demonstrate clear kinetic distinctions between these clusters. Quantification of AUC values revealed significantly higher glucose enrichment in *HG* + *HL* and *HG* + *LL* areas relative to *LG* + *HL* and *LG* + *LL* (Fig. 4G), and elevated lactate accumulation in *HG* + *HL* and *LG* + *HL* compared to *HG* + *LL* and *LG* + *LL* (Fig. 4H). *k*-means clustering and quantitative analyses conducted on a different cohort of colon cancer–bearing mice—10 CT26 tumor–implanted animals—using the same methods yielded similar results to those of the C26 strain (fig. S8).

To explore whether metabolic dynamics could be analyzed beyond static AUC features, a PCA-GMM framework was applied on

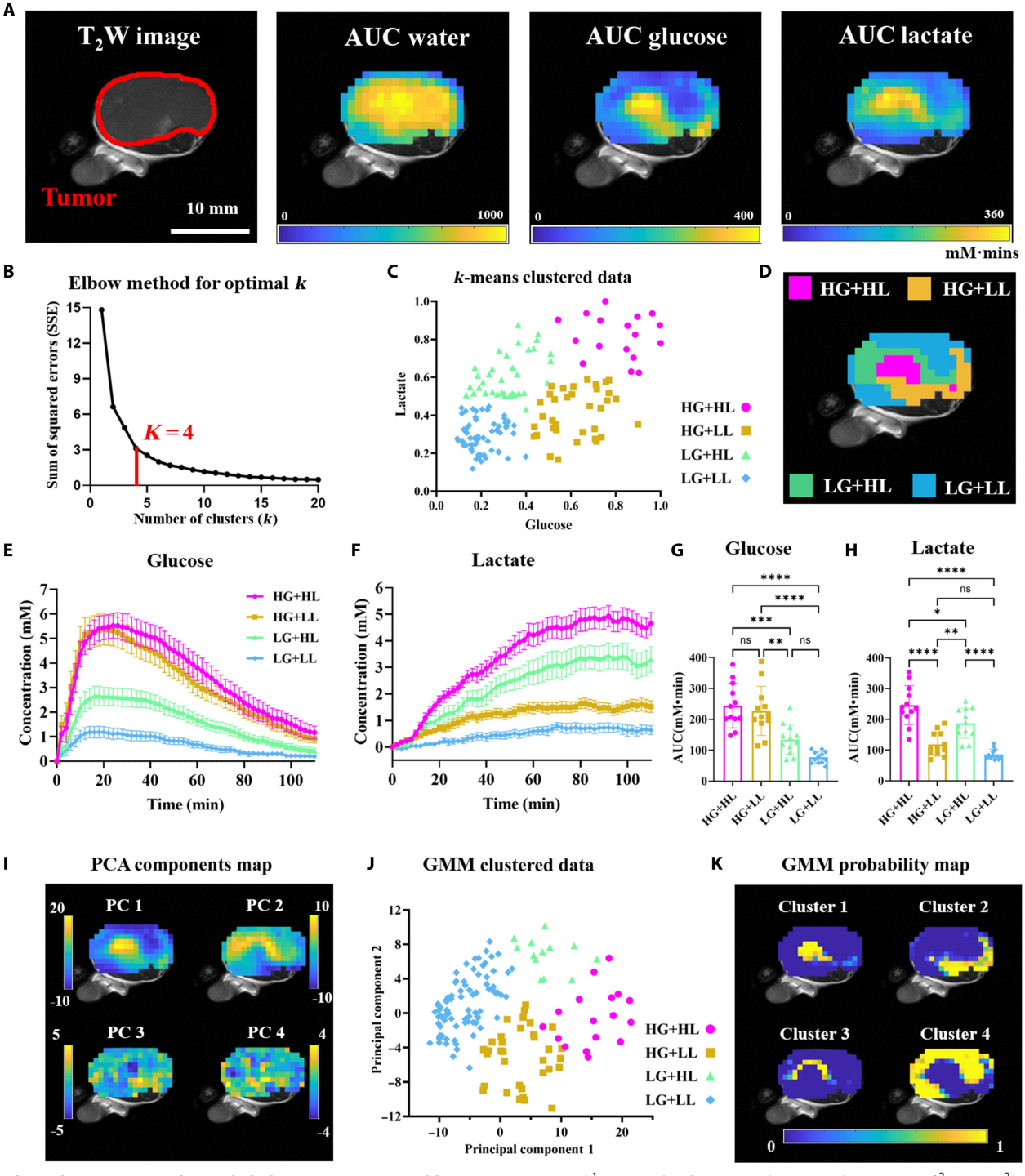


**Fig. 4. High-resolution DMI reveals metabolic heterogeneity in a viable C26 tumor.** (**A**) Axial $^{1}$H $T_2$-weighted anatomical image and AUC maps of $^{2}$H-water, $^{2}$H-glucose, and $^{2}$H-lactate. Water showed uniform distribution, whereas glucose and lactate exhibited pronounced spatial heterogeneity. (**B**) Elbow method identified four optimal clusters ($K = 4$) based on the sum of squared errors (SSE). (**C**) Voxel-wise distribution of normalized glucose and lactate AUC values following *k*-means clustering. (**D**) *k*-means clustering map of four metabolic phenotypes: *HG + HL* (high glucose, high lactate), *HG + LL* (high glucose, low lactate), *LG + HL* (low glucose, high lactate), and *LG + LL* (low glucose, low lactate). (**E** and **F**) Dynamic glucose (E) and lactate (F) concentration curves for each subregion of 12 C26 tumor–bearing mice. (**G** and **H**) Quantification of glucose (G) and lactate (H) AUC values across subregions of 12 C26 tumor–bearing mice. Glucose enrichment was significantly higher in *HG + HL* and *HG + LL* areas compared to *LG + HL* and *LG + LL* (*HG + HL*: 244.2 ± 20.77; *HG + LL*: 227.3 ± 22.94; *LG + HL*: 135.3 ± 14.04; *LG + LL*: 77.44 ± 5.56; ns: not significant, $^{**}P < 0.01$, $^{***}P < 0.01$, and $^{****}P < 0.0001$). Lactate accumulation was significantly elevated in *HG + HL* and *LG + HL* areas compared to *HG + LL* and *LG + LL* (*HG + HL*: 246.4 ± 18.32; *HG + LL*: 118.9 ± 11.11; *LG + HL*: 186.8 ± 14.07; *LG + LL*: 85.9 ± 4.92; $^{*}P < 0.05$, $^{**}P < 0.01$, $^{***}P < 0.001$, and $^{****}P < 0.0001$). (**I**) Spatial distribution of the first four principal components (PC1 to PC4) from PCA of the dynamic glucose and lactate time courses. (**J**) GMM clustering of voxels projected onto the first two PCs, showing distinct metabolic subregions. (**K**) GMM-derived probability maps illustrating soft classification of tumor voxels into four dynamic metabolic subregions.

the DMI data. The first four principal components extracted from the glucose and lactate time courses revealed dominant temporal variance patterns (Fig. 4I). GMM-based clustering in the reduced component space identified consistent phenotype groupings (Fig. 4J), and the resulting probability maps (Fig. 4K) yielded a soft classification of tumor voxels, reflecting continuous heterogeneity. Quantitative evaluations on the two *k*-means and PCA-GMM clustering methods (tables S1 and S2) show spatial features in common and demonstrate the capacity of high-resolution DMI to noninvasively resolve dynamic and spatially distinct metabolic phenotypes in viable, live tumors regardless of the statistics used in the analysis.

### DMI-defined metabolic subregions correspond closely with expression of metabolism-related markers

To validate the intratumoral heterogeneity revealed by high-resolution DMI, immunohistochemistry (IHC) was performed on the C26 tumor sections following in vivo imaging. $T_2$-weighted MR images were coregistered with corresponding histological sections to enable spatial correlation. Coregistration reliability was evaluated by calculating the Dice similarity coefficient (DSC); only good coregistration tumors (DSC $\geq$ 0.80) were included for downstream analysis, and poor coregistration tumors were discarded (fig. S9). Figure 5 shows results of one good coregistration example. The $T_2$-weighted MRI-defined areas (red contours) exhibited strong spatial concordance with histologically annotated areas (blue contours), providing a region-specific biochemical validation (Fig. 5C). IHC staining was performed for eight metabolism-related markers (*41*, *42*)—GLUT1, DLAT, LDHA, MCT4, PKM2, HIF-1α, MCT1, and AKT—to assess their spatial expression patterns across DMI-defined tumor subregions. DLAT was included as the E2 component of the pyruvate dehydrogenase complex (PDHC), representing a histology-accessible marker of mitochondrial pyruvate-oxidation machinery. The functional roles and associated metabolic pathways of these metabolism-related markers are summarized in table S3. On the basis of the voxel-wise in vivo clustering of glucose enrichment and lactate accumulation, the postmortem tumor was spatially segmented into the four metabolic subregions *HG* + *HL*, *HG* + *LL*, *LG* + *HL*, and *LG* + *LL* (Fig. 5C).

Four key metabolism-related markers—GLUT1, DLAT, MCT4, and LDHA—revealed distinct expression patterns across these DMI-defined subregions (Fig. 5D). Quantification of the integrated optical density (IOD) revealed significant differences in the expression of GLUT1, DLAT, LDHA, and MCT4 across the DMI-defined metabolic subregions (Fig. 5, E to H). GLUT1 and DLAT expression were significantly higher in *HG* areas than in *LG* areas, independent of lactate status. This finding supports a spatial association between DMI-defined glucose enrichment and glucose-handling/mitochondrial pyruvate-oxidation machinery, rather than directly proving increased intracellular glucose uptake or oxidative flux. In contrast, LDHA and MCT4 expression were significantly elevated in *HL* areas, supporting a spatial association between DMI-defined lactate signals and lactate-production/lactate-handling programs. Still, such local DMI lactate signals should be interpreted as reflecting a net labeled lactate pool determined by an interplay between production, retention, export, washout, and possible reutilization (table S4). Spatial correlation analyses (Fig. 5, I to L) further supported these findings: Glucose AUC was positively correlated with GLUT1 ($r = 0.7250$, $P < 0.001$) and DLAT ($r = 0.7092$, $P < 0.001$), while lactate AUC correlated with LDHA ($r = 0.7692$, $P < 0.001$) and MCT4 ($r = 0.7497$, $P < 0.001$). Together, these results establish a strong spatial and functional correspondence between DMI-defined metabolic phenotypes and the expression of key metabolism-related markers, validating the ability of DMI to noninvasively resolve biochemically distinct tumor subregions in vivo.

Four additional metabolism-related markers—PKM2, HIF-1α, MCT1, and AKT—were examined but did not show significant differences and/or correlations for the four subregions (fig. S10). In addition to these enzymatic results, IHC results based on IOD were further analyzed across all included C26 tumors with acceptable MRI-histology registration ($n = 8$), and a correlation analysis was conducted against the clustering quantitative results (AUC) obtained by DMI. The overall results were like those arising from the above-mentioned single tumors (fig. S11), showing statistically significant correlations as well.

### High-resolution DMI reveals intertumoral metabolic heterogeneities with different tumor subtypes

Accurate identification of tumor subtypes is essential for personalized cancer diagnosis, prognosis, and treatment selection. Conventional approaches such as biopsy followed by IHC or next-generation sequencing, though powerful, are invasive and subject to sampling bias. Therefore, we decided to explore whether quantitative descriptors of intratumoral metabolic heterogeneity could also discriminate tumor subtypes, thereby extending the analysis from intratumoral to intertumoral heterogeneity. To this end, two subtypes of colon cancer tumors, C26 and CT26, were selected and explored via receiver operating characteristic (ROC) analysis (*43*). Figure 6A illustrates the $T_2$-weighted images; DMI-derived water, glucose, and lactate signal maps; and the metabolic partitioning results obtained via *k*-means clustering for both tumor models. Quantitative analyses on the mean AUC values of glucose and lactate (Fig. 6, B and C) show that the mean AUC values of glucose and lactate in C26 tumors were statistically higher than those in CT26 tumors (glucose: C26, 163.2 ± 14.8; CT26, 86.21 ± 10.1; lactate: C26, 155.9 ± 9.8; CT26, 106.9 ± 13.5. $^{**}P < 0.01$, $^{***}P < 0.001$). ROC analyses (Fig. 6, D and E) also demonstrate that the mean AUC values have a clear ability of tumor classification (glucose: $AUC_{ROC} = 0.91$; lactate: $AUC_{ROC} = 0.83$). As in the preceding paragraph, the high-resolution nature of the DMI data was also combined here with unsupervised clustering, to quantify intratumoral heterogeneity using the high/low glucose and lactate AUC metrics separating distinct metabolic areas. Figure 6 (F and G) presents a quantitative comparison of glucose and lactate AUC (integrated concentrations) across distinct metabolic areas. The results reveal that glucose concentration in the *HG* + *HL* area was significantly higher in C26 tumors than in CT26 tumors ($P < 0.0001$), while lactate concentrations showed no statistically significant differences across areas. Figure 6H further compares the volumetric fractions of the distinct metabolic partitions within the entire tumor mass. This shows that the *LG* + *LL* region accounts for a significantly larger proportion of CT26 tumors than of C26 tumors ($P < 0.01$), further supporting the overall weaker metabolic activity characteristic of CT26.

To evaluate the predictive capability of these distinct metabolic features to differentiate tumor subtypes, ROC analyses were also performed on the clustered subregions. Figure 6 (I to M) displays the ROC curves with AUC values ($AUC_{ROC}$) greater than 0.8, including glucose concentration in the *HG* + *HL* region ($AUC_{ROC} = 0.92$), glucose concentration in the *LG* + *HL* area ($AUC_{ROC} = 0.82$), the fractional

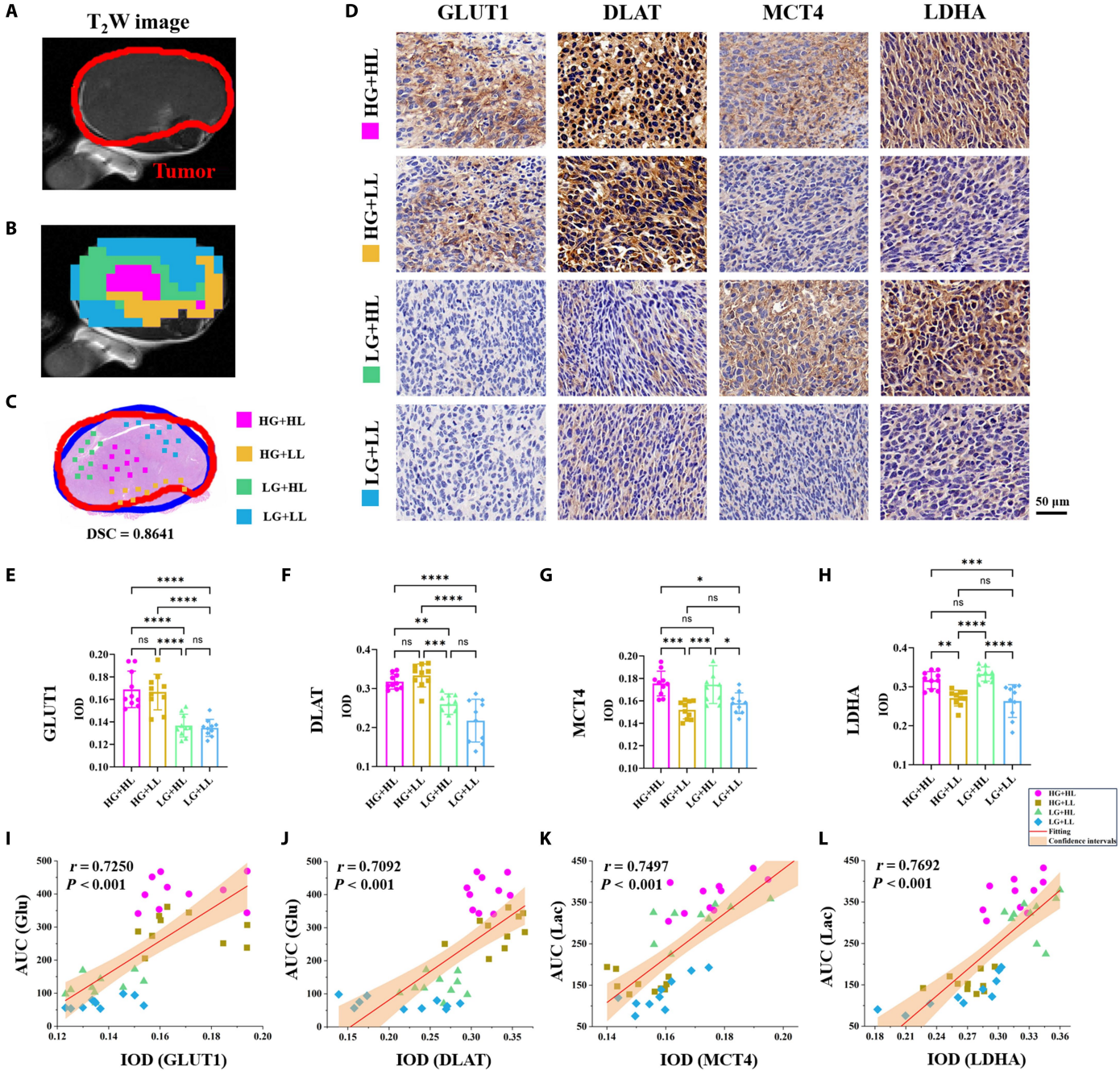


**Fig. 5. Spatial correspondences between DMI-defined metabolic subregions and metabolic metabolism-related markers.** (**A**) $T_2$-weighted anatomical MRI, which is the same source image as that shown in Fig. 4A and is reused here to facilitate direct comparison with the histological and immunohistochemical analyses. (**B**) DMI-based clustering map, which is the same source image as that shown in Fig. 4D and is reused here for comparison with the corresponding histological analysis. (**C**) Coregistration of the DMI-defined subregions (red contour) with histological sections (blue contour) enabled spatially matched IHC analysis. (**D**) Representative IHC staining images of GLUT1, DLAT, MCT4, and LDHA across the four subregions. Scale bar, 50 μm. (**E** to **H**) Quantification of marker expression based on IOD values. GLUT1 and DLAT levels were significantly higher in *HG* areas (E, GLUT1: *HG* + *HL*, 0.169 ± 0.005; *HG* + *LL*, 0.167 ± 0.005; *LG* + *HL*, 0.137 ± 0.003; *LG* + *LL*, 0.135 ± 0.002; F, DLAT: *HG* + *HL*, 0.318 ± 0.006; *HG* + *LL*, 0.334 ± 0.009; *LG* + *HL*, 0.260 ± 0.008; *LG* + *LL*, 0.22 ± 0.02), whereas MCT4 and LDHA were enriched in *HL* areas (G, LDHA: *HG* + *HL*, 0.317 ± 0.007; *HG* + *LL*, 0.271 ± 0.006; *LG* + *HL*, 0.333 ± 0.006; *LG* + *LL*, 0.26 ± 0.01; H, MCT4: *HG* + *HL*, 0.176 ± 0.003; *HG* + *LL*, 0.152 ± 0.003; *LG* + *HL*, 0.175 ± 0.005; *LG* + *LL*, 0.158 ± 0.003). Statistical significance: ns, not significant; **P* < 0.05, ***P* < 0.01, ****P* < 0.001, and *****P* < 0.0001. (**I** to **L**) Correlation between metabolite AUC and metabolism-related markers expression (IOD). Glucose AUC showed strong positive correlations with GLUT1 (I, $r = 0.7250$, $P < 0.001$) and DLAT (J, $r = 0.7092$, $P < 0.001$). Lactate AUC was significantly correlated with MCT4 (K, $r = 0.7497$, $P < 0.001$) and LDHA (L, $r = 0.7692$, $P < 0.001$). Shaded regions indicate 95% confidence intervals.

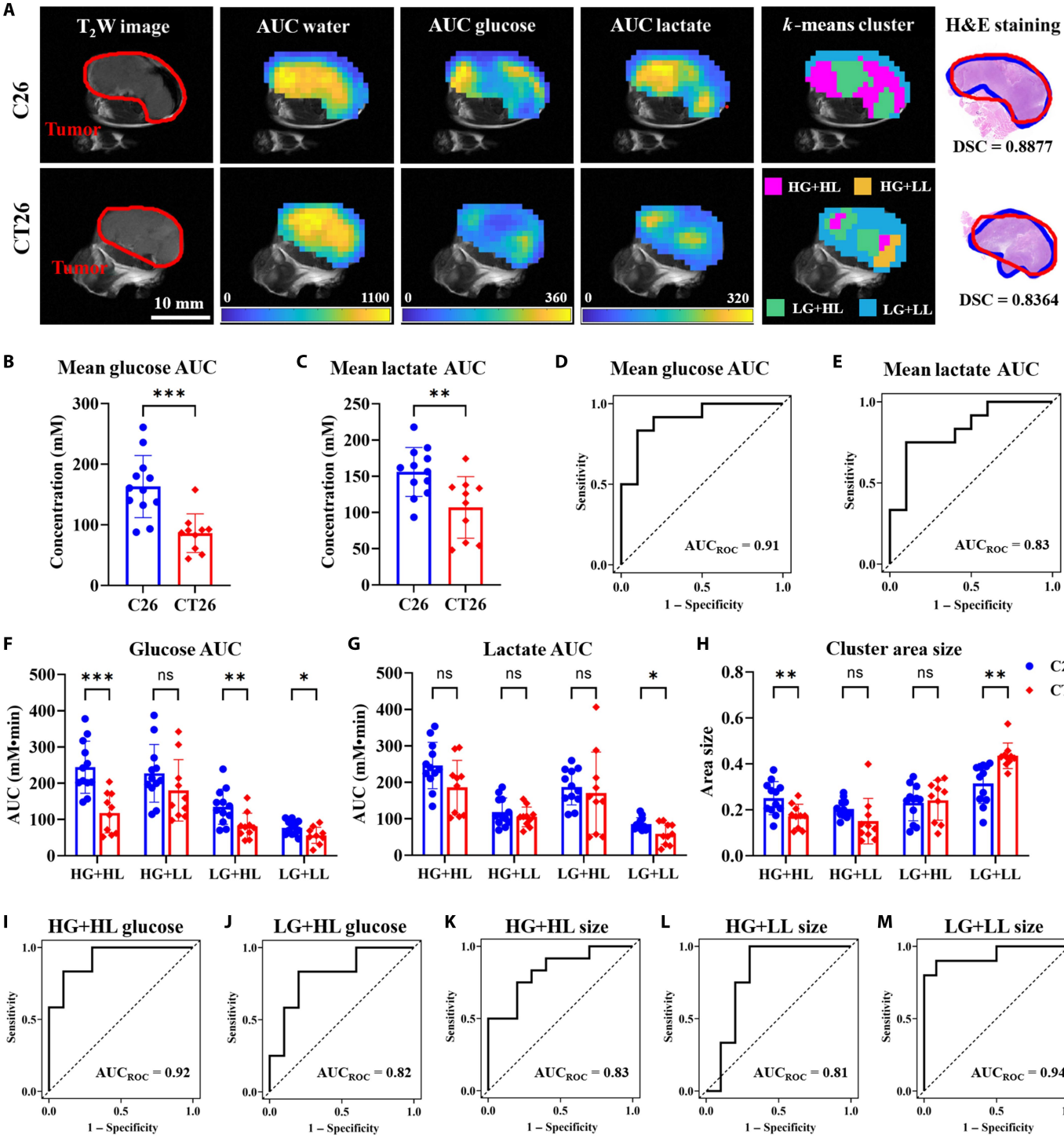


**Fig. 6. Differentiation of tumor subtypes (C26 and CT26) by DMI-defined intratumoral metabolic heterogeneities.** (**A**) Representative $T_2$-weighted anatomical images, DMI-derived AUC maps of water, glucose, and lactate, as well as *k*-means–based metabolic partitioning into four areas (*HG + HL*, *HG + LL*, *LG + HL*, and *LG + LL*) for the two indicated tumor subtypes. Corresponding H&E sections indicate limited overt necrosis in the representative tumors shown. (**B** and **C**) Statistical results of mean AUC values of glucose and lactate for the two tumor subtypes (**$P < 0.01$, ***$P < 0.001$). (**D** and **E**) ROC analyses of mean AUC values for glucose and lactate, showing a strong ability for tumor classification. (**F** to **H**) Quantitative analyses of glucose and lactate AUC values across distinct metabolic areas and their volumetric fractions within tumors, showing the presence or absence of statistical significance. (**I** to **M**) ROC curve analyses assessing the discriminative power of metabolic features for tumor subtype classification. Among these, glucose concentration in the *HG + HL* area (I) and the fractional volume of the *LG + LL* area (M) exhibited the highest predictive accuracy ($AUC_{ROC} = 0.92$ and 0.94, respectively).

size of the *HG* + *HL* region within the tumor ($AUC_{ROC} = 0.83$), the fractional size of *HG* + *LL* within the tumor ($AUC_{ROC} = 0.81$), and the fractional size of *LG* + *LL* within the tumor ($AUC_{ROC} = 0.94$; ROC curves for all features are provided in fig. S12). Among all these, the fractional size of the *LG* + *LL* region evidenced the strongest discriminative power, followed by glucose's concentration in the *HG* + *HL* region—highlighting again that maximal glucose enrichment and the extent of low-metabolic areas are key determinants distinguishing C26 from CT26 tumors. Further differences in the AUC distributions between the two tumor types are provided in fig. S13.

Last, supporting experiments on the individual cell strains were also performed (fig. S14), which as the DMI showed that C26 cells had stronger glycolysis (basal glycolysis: C26, 605.1 ± 24.0; CT26, 364.7 ± 40.0; compensatory glycolysis: C26, 1716.0 ± 44.1; CT26, 1674.0 ± 168.3; proton efflux rate from glycolysis: C26, 65.78 ± 1.06; CT26, 51.57 ± 1.46. ns, not significant, ***$P < 0.001$, ****$P < 0.0001$) and weaker mitochondrial respiration (basal respiration: C26, 268.1 ± 17.52, CT26, 363.8 ± 29.11; maximal respiration: C26, 386.5 ± 23.37; CT26, 584.3 ± 66.52; spare respiratory capacity: C26, 118.4 ± 8.93; CT26, 220.5 ± 38.71, *$P < 0.05$) than CT26 cells, indicating notable differences in metabolic activity.

## DISCUSSION

Metabolic heterogeneity is a defining feature of cancer biology, reflecting spatially variable nutrient delivery, pathway activity, cellular composition, and microenvironmental adaptation across tumor regions. In this study, we demonstrate that high–spatiotemporal resolution DMI based on MF-bSSFP can provide dynamic in vivo maps of labeled glucose enrichment and lactate generation in subcutaneous colorectal tumor models. When combined with unsupervised voxel-wise clustering, these maps delineated metabolically active and inactive compartments, resolved distinct glucose/lactate phenotypes within viable tumors, and yielded quantitative features that differed between C26 and CT26 tumors. These findings suggest that DMI-derived metabolic maps can serve as candidate imaging features for characterizing intratumoral heterogeneity and model-dependent intertumoral metabolic differences. The spatial correspondence between DMI-defined phenotypes and histological/IHC features further supports the biological relevance of these imaging-defined subregions, while also emphasizing the need for cautious interpretation of the underlying mechanisms.

The ability to resolve these metabolic phenotypes was enabled by the MF-bSSFP DMI acquisition. Similar to other bSSFP-based DMI approaches (*34*, *44*), MF-bSSFP exploits the high signal efficiency of balanced steady-state acquisitions and the relative sparsity of the $^2H$ spectrum. However, rather than relying on full spectroscopic encoding or long free induction decay readouts, MF-bSSFP acquires images at optimized frequency offsets and uses metabolite-specific magnitude/phase responses for multicomponent reconstruction. This design enables robust separation of water, glucose, and lactate while maintaining high in-plane spatial resolution. By maintaining a short TR and using multi-offset encoding with iterative off-resonance correction, MF-bSSFP also reduces the vulnerability to banding artifacts and metabolite cross-talk that can become more pronounced in longer-TR CSI-bSSFP or ME-bSSFP implementations (figs. S15 and S16). These features make MF-bSSFP particularly suitable for high-resolution DMI of sparse metabolite systems, such as the glucose-to-lactate labeling experiment studied here.

Because glucose and lactate signals report different stages of the labeled-glucose metabolic process, they require different biological interpretations. The *HG*/*LG* axis represents apparent $^2H$-glucose enrichment within each voxel. Following a bolus administration of [6,6′-$^2H_2$]glucose, the signal that is observed reflects a mixed glucose pool including vascular, extracellular, and intracellular components. Therefore, high glucose enrichment should not be interpreted as a direct compartment-specific measure of intracellular glucose uptake alone; it may also reflect substrate delivery, vascular volume, interstitial distribution, or perfusion-related effects. By contrast, $^2H$-lactate arises from an enzymatic conversion of labeled glucose, and is therefore closely related to downstream glycolytic processing. Even so, the local lactate signal should still be viewed as a net labeled lactate pool shaped by production, retention, washout, and/or potential reutilization of the deuterated metabolite. This distinction motivated our two-axis framework, in which *HG*/*LG* describes substrate enrichment and availability, whereas *HL*/*LL* describes labeled lactate accumulation. Hydrogen deuterium oxide (HDO) was not used as a primary clustering feature because it reflects a mixture of systemic label accumulation, vascular water content, tissue exchange, and local metabolism; consistent with this interpretation, including HDO AUC did not substantially alter the clustering results.

This distinction between glucose enrichment and lactate accumulation is important for interpreting the IHC associations. These associations should be regarded as spatial phenotype correlations rather than direct mechanistic proof. Higher GLUT1 expression in *HG* regions supports the biological relevance of the glucose-enriched phenotype, but GLUT1 is unlikely to be the sole determinant of the measured glucose signal because vascular delivery and extracellular glucose pools may also contribute. DLAT, the E2 component of the PDHC, is interpreted here as a histology-accessible marker of mitochondrial pyruvate-oxidation machinery rather than as a direct measurement of oxidative flux, particularly because reliable Glx mapping was not achieved. Similarly, LDHA and MCT4 enrichment in lactate-associated regions supports a spatial relationship between DMI-defined lactate phenotypes and lactate-production/handling programs, but does not establish a one-to-one causal relationship with local lactate concentration. LDHA reflects lactate-producing capacity, whereas MCT4 mediates lactate export and could, under some conditions, reduce intracellular lactate retention. Thus, the IHC findings support the biological plausibility of the DMI-defined subregions while indicating that the underlying mechanisms are likely multifactorial.

The model-dependent differences between C26 and CT26 tumors should be interpreted as tissue-level metabolic phenotypes rather than direct molecular subtype assignments. DMI-derived glucose and lactate features, including both mean metabolic AUCs and cluster-based heterogeneity descriptors, differed between these two colorectal tumor models, consistent with the broader concept that colorectal cancers can exhibit distinct metabolic, immune, and stromal phenotypes. However, high-resolution DMI provides a spatial readout of glucose enrichment and lactate labeling, not a direct molecular classification. These DMI phenotypes should therefore be viewed as integrated tumor-microenvironment metabolic states involving cancer cells, immune cells, stromal components, vascular delivery, and extracellular metabolite pools. This is particularly relevant because previous immune profiling studies reported that CT26 tumors are more immune-infiltrated than Colon 26/C26 tumors, including a higher fraction of $CD45^+$ immune cells, and exhibit different sensitivity to therapy targeting programmed cell death protein 1 (*45*). Immune

cells can consume glucose and participate in lactate metabolism, whereas tumor-derived lactate and extracellular acidification can modulate immune-cell function and contribute to immunosuppressive niches. Future studies combining DMI with spatial immune profiling will be important for determining how DMI-defined glucose and lactate phenotypes relate to immune infiltration and immunotherapy response.

Several limitations remain. First, although MF-bSSFP achieved an in-plane resolution of 0.9 mm × 0.9 mm, the current acquisition used a 6-mm slice thickness. Histological and IHC sections of 4-μm thickness were obtained near the central imaging plane and were used for central-plane spatial validation rather than complete volumetric validation. Representative serial H&E sections across the DMI slice showed broadly consistent large-scale viable and necrotic tissue patterns (fig. S17), but each histological section still represents only a small fraction of the full DMI slice volume. Future 3D MF-bSSFP DMI with improved through-plane resolution will be important for more comprehensive volumetric assessment. Second, IHC validation was performed only in the C26 model and was designed as a within-tumor spatial validation rather than a comprehensive molecular comparison between C26 and CT26 tumors. Extending IHC, immune profiling, and spatial molecular analyses to both models will be necessary to clarify the biological mechanisms underlying the model-dependent DMI phenotypes. Third, no reliable Glx resonance was detected under the present high-resolution spectra (fig. S18). Therefore, oxidative metabolism was not quantified directly by DMI-derived Glx signals, and DLAT was used only as a histological proxy of mitochondrial pyruvate-oxidation machinery. Last, MF-bSSFP is best suited to relatively sparse spectra with known and separable resonances. Applications involving more crowded spectra, lower magnetic fields, or additional deuterated substrates may require more sophisticated spectral modeling, $B_0$ correction, and reconstruction constraints.

Together, these findings establish high-resolution MF-bSSFP DMI as a promising approach for noninvasively resolving spatial metabolic heterogeneity in vivo. By combining dynamic glucose/lactate mapping with unsupervised phenotype analysis, this framework provides tissue-level metabolic information that complements histology, IHC, and molecular profiling. Future integration with DCE MRI, diffusion MRI, Glx-sensitive DMI protocols, and spatial immune or molecular profiling should further improve the biological interpretability of DMI-derived phenotypes and support their application in treatment response assessment and precision oncology.

## METHODS

### Theory

For each metabolite, the bSSFP signal can be derived from the Bloch equations and presented as (*46*, *47*)

$$\mathrm{MS} = \frac{ae^{i2\pi(f_b+f_m)\mathrm{TR}} + b}{c\cos\left(2\pi\left(f_b+f_m\right)\mathrm{TR}\right) + d} \tag{1}$$

where $a = -\sin\alpha\left(1-E_1\right)E_2$, $b = \sin\alpha\left(1-E_1\right)$, $c = E_2\left(1-E_1\right)(1+\cos\alpha)$, and $d = 1 - E_1\cos\alpha - E_2^2\left(E_1-\cos\alpha\right)$. Here, $E_1 = e^{-\frac{\mathrm{TR}}{T_1}}$ and $E_2 = e^{-\frac{\mathrm{TR}}{T_2}}$ depend on the TR and relaxation times $T_1$ and $T_2$, α is the RF flip angle, $f_b$ is the frequency offsets caused by magnetic field inhomogeneities, and $f_m$ is the chemical shift (in frequency units). On the basis of this model, the bSSFP signal is the summation of the magnitude and phase profile for each metabolite spectral component determined as

$$S_n = e^{i2\pi f_b \mathrm{TE}} \sum_{m=1}^{M} \rho_m \mathrm{MS}_m e^{i2\pi\left(f_m+f_n\right)\mathrm{TE}} \tag{2}$$

where $\rho_m$ is the initial signal intensity of the metabolite, and $f_n$ is the user-defined pulse frequency offsets. The formula shows that the steady-state magnetization vector of the metabolite is modulated not only by its own chemical shift but also by the frequency of the pulse; this will define a characteristic frequency response featuring periodic nulls and passbands as determined by the TR, flip angle, and $T_1$ and $T_2$ values of the tissue present. We use this to separate different metabolic images, by acquiring bSSFP data at various frequency offsets $n = 1, 2, \ldots, N$. The ensuing signals can be represented by Eq. 3

$$\mathbf{S} = \mathbf{A}\boldsymbol{\rho} \tag{3}$$

where $\boldsymbol{S} = \left[S_1\, S_2 \cdots S_{N-1}\, S_N\right]^T$, $\boldsymbol{\rho} = \left[\rho_1\, \rho_2 \cdots \rho_{M-1}\, \rho_M\right]^T$, and the coefficient matrix $\mathbf{A}$ with $N$ rows and $M$ columns can be calculated using Eq. 2. Using a least-squares fitting approach for linear systems of equations, the metabolic signals can be found by the pseudo-inverse calculation

$$\boldsymbol{\rho} = \left(\mathbf{A}^{\mathrm{T}}\mathbf{A}\right)^{-1}\mathbf{A}^{\mathrm{T}}\mathbf{S} \tag{4}$$

Although the metabolite distribution can theoretically be solved using the least-squares method, the presence of the unknown magnetic field inhomogeneity in the $\mathbf{A}$ matrix poses a challenge. In this work, we used two techniques to overcome the difficulties associated with the least-squares method: (i) measuring the $B_0$ field map using the $^1$H-ME_GRE sequence, and (ii) adopting an iterative reconstruction approach. For more details, please refer to section S1.

### Phantom experiments

Three metabolite phantoms ($^2H_2O$: ~40 mM, deuterated glucose: ~20 mM; and deuterated lactate: ~20 mM) were prepared to evaluate the SNR improvement of MF-bSSFP. All experiments were acquired on a Bruker BioSpin 9.4-T MRI scanner, and the $^2$H coils were homemade surface coils nested inside a 72-mm $^1$H volume coil. Before the $^2$H experiments, $^1$H structural images of the phantoms were acquired using the rapid acquisition with relaxation enhancement (RARE) sequence with the following parameters: TR = 2500 ms, effective TE = 24 ms, flip angle = 90°, number of averages = 4, field of view (FOV) = 30 × 30 mm$^2$, matrix = 160 × 160, number of slices = 9, and slice thickness = 2 mm. Afterward, $^2$H images were acquired using the MF-bSSFP with the following parameters: TR = 3.4 ms, flip angle = 40°, number of averages = 512, FOV = 30 × 30 mm$^2$, matrix = 32 × 32, number of slices = 1, and slice thickness = 4 mm; five frequency offsets: −190, −110, 0, 110, and 190 Hz; scan time: 4 min 39 s. To compare with other methods, we also acquired images of conventional CSI and CSI-bSSFP with the following parameters: FOV = 30 × 30 mm$^2$, matrix = 32 × 32, number of slices = 1, and slice thickness = 4 mm; spectral bandwidth/points: CSI, 2000 Hz/128 points and CSI-bSSFP, 4065 Hz/64 points; scan time: CSI, 4 min 24 s and CSI-bSSFP, 4 min 32 s.

### Animal protocol and procedures

All animal procedures were approved by the Animal Care and Use Committee of the Innovation Academy for Precision Measurement Science and Technology, Chinese Academy of Sciences (APM23022T) and were conducted according to the National Institutes of Health animal care guidelines. BALB/c mice (male, 5 to 6 weeks) were purchased from Beijing Vital River Laboratory Animal Technology Co., Ltd. (Beijing, China), and the colon cancer mouse model was established using C26 and CT26 cells obtained from Wuhan Servicebio Technology Co. Ltd. (Wuhan, China). The mice were housed in a specific pathogen–free animal room with a 12-hour/12-hour light-dark cycle and automatically controlled temperature and humidity.

The overall experimental workflow is shown in fig. S19. A total of 30 tumor-bearing mice were used to establish two subcutaneous colorectal tumor models: C26 ($n = 15$) and CT26 ($n = 15$). During tumor growth, one C26 tumor–bearing mouse and two CT26 tumor–bearing mice died before or during imaging. All remaining mice underwent DMI scanning and H&E staining. Among these animals, two C26 tumors and three CT26 tumors showed extensive necrosis and were used for the viable/necrotic compartment analysis. The remaining tumors without extensive necrosis, including 12 C26 and 10 CT26 tumors, were used for metabolic phenotype clustering and ROC analysis to evaluate intratumoral metabolic heterogeneity and between-model differences. IHC analysis was performed only in the C26 model. Among the 12 C26 tumors used for IHC staining, 4 were excluded from quantitative MRI-histology correlation because reliable spatial registration could not be achieved due to section deformation, cutting-plane mismatch, or poor boundary correspondence. The remaining eight C26 tumors with acceptable MRI-histology alignment were included in the final correlation analysis between DMI-defined metabolic subregions and metabolism-related marker expression.

### In vivo imaging

Mice were preanesthetized with isoflurane before scanning. After injecting an indwelling needle into their tail vein, mice were placed supine on the 9.4-T MRI scanning bed. The body temperature was stabilized at 38°C with water circulation. After fixing the mice and the coil, the MRI scan was started. During the scanning process, the oxygen flow meter for anesthesia control was adjusted to 0.5 liters/min, and the anesthetic gas isoflurane concentration was maintained at approximately 1.5%. Throughout the scanning process, the respiratory rate of the mice was continuously monitored and maintained at approximately 45 breaths/min.

For the DMI, [6,6′-$^2H_2$]glucose (Cambridge Isotopes Laboratories Inc., USA) was dissolved in sterile saline and administered via a tail vein catheter at a dose of 2 g/kg body weight. The solution was delivered as a controlled bolus injection over approximately 60 s. Dynamic $^2$H-MRSI acquisition was initiated immediately before the injection and continued for 100 min thereafter.

$^2$H data were acquired using a dedicated single-tuned $^2$H surface coil (diameter, 18 mm) positioned over the tumor. For anatomical localization and shimming, a separate $^1$H volume coil (orthogonal, two-channel) with an inner diameter of 72 mm was used. Structural images were acquired using RARE sequences with the following parameters: TR = 2500 ms, effective TE = 24 ms, flip angle = 90°, number of averages = 4, FOV = 30 × 30 mm$^2$, matrix = 160 × 160, number of slices = 9, and slice thickness = 2 mm. Then, local shimming was performed, with the full width at half maximum of the water peak in the $^1$H spectrum maintained between 30 and 50 Hz for each experiment. After shimming, $B_0$ field maps were acquired for the subsequent data processing. Subsequently, before the injection, nonlocalized spectroscopy (NSPECT) and MF-bSSFP imaging data were acquired as baseline. The NSPECT scanning parameters were as follows: TR = 66 ms, flip angle = 30°, number of averages = 512, spectral bandwidth/number of points = 2000 Hz/128 points, slice thickness = 6 mm, and scan time = 33 s. The MF-bSSFP scanning parameters were as follows: TR = 3.4 ms, flip angle = 40°, number of averages = 1100, FOV = 30 × 30 mm$^2$, matrix = 32 × 32, number of slices = 1, slice thickness = 6 mm; five frequency offsets: −190, −110, 0, 110, and 190 Hz; every frequency offset scan time = 2 min.

### Unsupervised voxel-wise clustering

Clustering analyses were implemented using MATLAB (R2014a, MathWorks, Natick, MA). First, DMI was used to obtain the metabolic images of deuterated glucose and deuterated lactate in tumor tissues. For *k*-means clustering, the AUC of the metabolic curves of deuterated glucose and lactate was calculated; *k*-means clustering on the AUC value of each pixel was then performed, and the optimal number of clusters (*K* value) in *k*-means clustering was done using the "elbow" method (*48*). The tumor areas could then be divided into four metabolic subregions using the optimal *K* value. For PCA + GMM analysis, the 56-dimensional dynamic images of deuterated glucose and deuterated lactic acid were respectively reduced to 10-dimensional principal component images through PCA. Subsequently, GMM clustering was performed on the 10-dimensional principal component images, and lastly, the probability density distribution maps of the four metabolic subregions were obtained.

### Immunohistochemical analysis

Tumor tissues from all animals were collected after completion of the $^2$H MRI/MRSI scans and fixed in a 4% paraformaldehyde solution. After fixation, the tumor tissues were embedded in paraffin and subsequently sectioned into 4-μm-thick slices for staining. After deparaffinization, the sections were stained with H&E solution. H&E staining was performed for all tumors. IHC staining for metabolism-related markers was performed in the C26 cohort, and only tumors with good MRI-histology spatial alignment were included in the final spatial correlation analysis. For IHC evaluation, primary antibodies (Proteintech, Rosemont, IL) against LDHA, HIF-1α, PKM2, DLAT, GLUT1, AKT, MCT1, and MCT4 were used for detection. HE and IHC images were acquired using an Olympus FSX100 microscope (Olympus, Tokyo, Japan), scanned with a Pannoramic MIDI scanner (3DHISTECH, Budapest, Hungary), and analyzed using Image-Pro Plus software (version 6.0, Media Cybernetics, Rockville, MD, USA; U12388-02, HAMAMATSU, Hamamatsu City, Japan).

### Data processing and analysis

The magnetic resonance spectra acquired by NSPECT were zero-filled and fitted using the AMARES toolbox in MATLAB (R2014a, MathWorks, Natick, MA), with the fit constrained based on known information about relative chemical shifts and linewidths. The metabolite peaks obtained from the fit were converted to concentrations based on the 10.12 mM $^2$H-labeled natural abundance water concentration and the corresponding $T_1/T_2$ values. Data for CSI images were obtained by applying zero-filling, matched-weighting filters (3 Hz apodization) in the spectral domain, and 3D Fourier transform. For the experimental data obtained from phantoms and animal models acquired by bSSFP, magnitude and phase images were extracted,

and images of water, glucose, and lactate were reconstructed using the algorithm proposed in section S1, implemented in MATLAB.

Statistical and graphical analyses were performed using Prism v9.0 (GraphPad). Comparisons among multiple groups were conducted using one-way and two-way analysis of variance (ANOVA). Pearson correlation coefficient was used to analyze the correlation between imaging and pathology. Statistical significance was set at $P < 0.05$ after correction for multiple comparisons.

## Supplementary Materials

**This PDF file includes:**

Supplementary Text
Figs. S1 to S19
Tables S1 to S4

## REFERENCES


1. N. El-Sayes, A. Vito, K. Mossman, Tumor heterogeneity: A great barrier in the age of cancer immunotherapy. *Cancers* **13**, 806 (2021).
2. M. Demicco, X.-Z. Liu, K. Leithner, S.-M. Fendt, Metabolic heterogeneity in cancer. *Nat. Metab.* **6**, 18–38 (2024).
3. C. T. Hensley, B. Faubert, Q. Yuan, N. Lev-Cohain, E. Jin, J. Kim, L. Jiang, B. Ko, R. Skelton, L. Loudat, M. Wodzak, C. Klimko, E. McMillan, Y. Butt, M. Ni, D. Oliver, J. Torrealba, C. R. Malloy, K. Kernstine, R. E. Lenkinski, R. J. DeBerardinis, Metabolic heterogeneity in human lung tumors. *Cell* **164**, 681–694 (2016).
4. J. Kim, R. J. DeBerardinis, Mechanisms and implications of metabolic heterogeneity in cancer. *Cell Metab.* **30**, 434–446 (2019).
5. I. Dagogo-Jack, A. T. Shaw, Tumour heterogeneity and resistance to cancer therapies. *Nat. Rev. Clin. Oncol.* **15**, 81–94 (2018).
6. B. Faubert, A. Solmonson, R. J. DeBerardinis, Metabolic reprogramming and cancer progression. *Science* **368**, eaaw5473 (2020).
7. P. L. Bedard, A. R. Hansen, M. J. Ratain, L. L. Siu, Tumour heterogeneity in the clinic. *Nature* **501**, 355–364 (2013).
8. P. R. Prasetyanti, J. P. Medema, Intra-tumor heterogeneity from a cancer stem cell perspective. *Mol. Cancer* **16**, 41 (2017).
9. M. Proietto, M. Crippa, C. Damiani, V. Pasquale, E. Sacco, M. Vanoni, M. Gilardi, Tumor heterogeneity: Preclinical models, emerging technologies, and future applications. *Front. Oncol.* **13**, 1164535 (2023).
10. P. Gangadaran, R. L. Rajendran, B.-C. Ahn, Application of in vivo imaging techniques for monitoring natural killer cell migration and tumor infiltration. *Cancers* **12**, 1318 (2020).
11. H. J. W. L. Aerts, E. R. Velazquez, R. T. H. Leijenaar, C. Parmar, P. Grossmann, S. Carvalho, J. Bussink, R. Monshouwer, B. Haibe-Kains, D. Rietveld, F. Hoebers, M. M. Rietbergen, C. R. Leemans, A. Dekker, J. Quackenbush, R. J. Gillies, P. Lambin, Decoding tumour phenotype by noninvasive imaging using a quantitative radiomics approach. *Nat. Commun.* **5**, 4006 (2014).
12. R. Weissleder, M. J. Pittet, Imaging in the era of molecular oncology. *Nature* **452**, 580–589 (2008).
13. D. A. Mankoff, A definition of molecular imaging. *J. Nucl. Med.* **48**, 18N–21N (2007).
14. M. G. V. Heiden, L. C. Cantley, C. B. Thompson, Understanding the Warburg effect: The metabolic requirements of cell proliferation. *Science* **324**, 1029–1033 (2009).
15. M. V. Liberti, J. W. Locasale, The Warburg effect: How does it benefit cancer cells? *Trends Biochem. Sci.* **41**, 211–218 (2016).
16. S. Chicklore, V. Goh, M. Siddique, A. Roy, P. K. Marsden, G. J. Cook, Quantifying tumour heterogeneity in $^{18}$F-FDG PET/CT imaging by texture analysis. *Eur. J. Nucl. Med. Mol. Imaging* **40**, 133–140 (2013).
17. C. Bailly, C. Bodet-Milin, M. Bourgeois, S. Gouard, C. Ansquer, M. Barbaud, J.-C. Sébille, M. Chérel, F. Kraeber-Bodéré, T. Carlier, Exploring tumor heterogeneity using PET imaging: The big picture. *Cancers* **11**, 1282 (2019).
18. H. M. De Feyter, R. A. de Graaf, Deuterium metabolic imaging—Back to the future. *J. Magn. Reson.* **326**, 106932 (2021).
19. F. Pan, X. Liu, J. Wan, Y. Guo, P. Sun, X. Zhang, J. Wang, Q. Bao, L. Yang, Advances and prospects in deuterium metabolic imaging (DMI): A systematic review of in vivo studies. *Eur. Radiol. Exp.* **8**, 65 (2024).
20. H. M. De Feyter, K. L. Behar, Z. A. Corbin, R. K. Fulbright, P. B. Brown, S. McIntyre, T. W. Nixon, D. L. Rothman, R. A. de Graaf, Deuterium metabolic imaging (DMI) for MRI-based 3D mapping of metabolism in vivo. *Sci. Adv.* **4**, eaat7314 (2018).
21. Y. Zhao, Y. Li, W. Jin, R. Guo, C. Ma, W. Tang, Y. Li, G. El Fakhri, Z.-P. Liang, Ultrafast J-resolved magnetic resonance spectroscopic imaging for high-resolution metabolic brain imaging. *Nat. Biomed. Eng.* **9**, 1835–1847 (2025).
22. W. Bogner, R. Otazo, A. Henning, Accelerated MR spectroscopic imaging—A review of current and emerging techniques. *NMR Biomed.* **34**, e4314 (2021).
23. J. M. Goldenberg, M. D. Pagel, Assessments of tumor metabolism with CEST MRI. *NMR Biomed.* **32**, e3943 (2019).
24. S. E. Day, M. I. Kettunen, F. A. Gallagher, D.-E. Hu, M. Lerche, J. Wolber, K. Golman, J. H. Ardenkjaer-Larsen, K. M. Brindle, Detecting tumor response to treatment using hyperpolarized 13C magnetic resonance imaging and spectroscopy. *Nat. Med.* **13**, 1382–1387 (2007).
25. K. M. Brindle, S. E. Bohndiek, F. A. Gallagher, M. I. Kettunen, Tumor imaging using hyperpolarized $^{13}$C magnetic resonance spectroscopy. *Magn. Reson. Med.* **66**, 505–519 (2011).
26. P. C. van Zijl, K. Brindle, H. Lu, P. B. Barker, R. Edden, N. Yadav, L. Knutsson, Hyperpolarized MRI, functional MRI, MR spectroscopy and CEST to provide metabolic information in vivo. *Curr. Opin. Chem. Biol.* **63**, 209–218 (2021).
27. J. D. Kaggie, A. S. Khan, T. Matys, R. F. Schulte, M. J. Locke, A. Grimmer, A. Frary, I. Horvat Menih, E. Latimer, M. J. Graves, M. A. McLean, F. A. Gallagher, Deuterium metabolic imaging and hyperpolarized $^{13}$C-MRI of the normal human brain at clinical field strength reveals differential cerebral metabolism. *Neuroimage* **257**, 119284 (2022).
28. E. T. Montrazi, K. Sasson, L. Agemy, A. Scherz, L. Frydman, Molecular imaging of tumor metabolism: Insight from pyruvate- and glucose-based deuterium MRI studies. *Sci. Adv.* **10**, eadm8600 (2024).
29. J. Chen Ming Low, A. J. Wright, F. Hesse, J. Cao, K. M. Brindle, Metabolic imaging with deuterium labeled substrates. *Prog. Nucl. Magn. Reson. Spectrosc.* **134-135**, 39–51 (2023).
30. M. Straathof, A. E. Meerwaldt, H. M. De Feyter, R. A. de Graaf, R. M. Dijkhuizen, Deuterium metabolic imaging of the healthy and diseased brain. *Neuroscience* **474**, 94–99 (2021).
31. F. Kreis, A. J. Wright, F. Hesse, M. Fala, D.-e. Hu, K. M. Brindle, Measuring tumor glycolytic flux in vivo by using fast deuterium MRI. *Radiology* **294**, 289–296 (2020).
32. F. Hesse, V. Somai, F. Kreis, F. Bulat, A. J. Wright, K. M. Brindle, Monitoring tumor cell death in murine tumor models using deuterium magnetic resonance spectroscopy and spectroscopic imaging. *Proc. Natl. Acad. Sci. U.S.A.* **118**, e2014631118 (2021).
33. D. C. Peters, S. Markovic, Q. Bao, D. Preise, K. Sasson, L. Agemy, A. Scherz, L. Frydman, Improving deuterium metabolic imaging (DMI) signal-to-noise ratio by spectroscopic multi-echo bSSFP: A pancreatic cancer investigation. *Magn. Reson. Med.* **86**, 2604–2617 (2021).
34. E. T. Montrazi, K. Sasson, L. Agemy, D. C. Peters, O. Brenner, A. Scherz, L. Frydman, High-sensitivity deuterium metabolic MRI differentiates acute pancreatitis from pancreatic cancers in murine models. *Sci. Rep.* **13**, 19998 (2023).
35. S. Markovic, T. Roussel, L. Agemy, K. Sasson, D. Preise, A. Scherz, L. Frydman, Deuterium MRSI characterizations of glucose metabolism in orthotopic pancreatic cancer mouse models. *NMR Biomed.* **34**, e4569 (2021).
36. G. Batsios, C. Taglang, M. Tran, N. Stevers, C. Barger, A. M. Gillespie, S. M. Ronen, J. F. Costello, P. Viswanath, Deuterium metabolic imaging reports on TERT expression and early response to therapy in cancer. *Clin. Cancer Res.* **28**, 3526–3536 (2022).
37. R. V. Simões, R. N. Henriques, B. M. Cardoso, F. F. Fernandes, T. Carvalho, N. Shemesh, Glucose fluxes in glycolytic and oxidative pathways detected in vivo by deuterium magnetic resonance spectroscopy reflect proliferation in mouse glioblastoma. *Neuroimage Clin.* **33**, 102932 (2022).
38. J. C. M. Low, J. Cao, F. Hesse, A. J. Wright, A. Tsyben, I. Alshamleh, R. Mair, K. M. Brindle, Deuterium metabolic imaging differentiates glioblastoma metabolic subtypes and detects early response to chemoradiotherapy. *Cancer Res.* **84**, 1996–2008 (2024).
39. R. V. Simões, R. N. Henriques, J. L. Olesen, B. M. Cardoso, F. F. Fernandes, M. A. V. Monteiro, S. N. Jespersen, T. Carvalho, N. Shemesh, Deuterium metabolic imaging phenotypes mouse glioblastoma heterogeneity through glucose turnover kinetics. *eLife* **13**, RP100570 (2025).
40. C. Taglang, G. Batsios, J. Mukherjee, M. Tran, A. M. Gillespie, D. Hong, S. M. Ronen, H. Artee Luchman, R. O. Pieper, P. Viswanath, Deuterium magnetic resonance spectroscopy enables noninvasive metabolic imaging of tumor burden and response to therapy in low-grade gliomas. *Neuro Oncol.* **24**, 1101–1112 (2022).
41. W. Xu, J. Weng, M. Xu, Q. Zhou, S. Liu, Z. Hu, N. Ren, C. Zhou, Y. Shen, Functions of key enzymes of glycolytic metabolism in tumor microenvironment. *Cell. Reprogram.* **25**, 91–98 (2023).
42. A. Herling, M. König, S. Bulik, H. G. Holzhütter, Enzymatic features of the glucose metabolism in tumor cells. *FEBS J.* **278**, 2436–2459 (2011).
43. A. Linden, Measuring diagnostic and predictive accuracy in disease management: An introduction to receiver operating characteristic (ROC) analysis. *J. Eval. Clin. Pract.* **12**, 132–139 (2006).
44. X. Liu, Q. Bao, Z. Liu, J. Wang, M. Otikovs, Z. Zhang, X. Cheng, J. Wang, L. Frydman, X. Zhou, M. Liu, C. Liu, Exploring metabolic aberrations after intracerebral hemorrhage in vivo with deuterium metabolic spectroscopy imaging. *Anal. Chem.* **96**, 15563–15571 (2024).
45. Y. Sato, Y. Fu, H. Liu, M. Y. Lee, M. H. Shaw, Tumor-immune profiling of CT-26 and Colon 26 syngeneic mouse models reveals mechanism of anti-PD-1 response. *BMC Cancer* **21**, 1222 (2021).

46. K. Scheffler, S. Lehnhardt, Principles and applications of balanced SSFP techniques. *Eur. Radiol.* **13**, 2409–2418 (2003).
47. K. L. Miller, Asymmetries of the balanced SSFP profile. Part I: Theory and observation. *Magn. Reson. Med.* **63**, 385–395 (2010).
48. R. Sammouda, A. El-Zaart, An optimized approach for prostate image segmentation using k-means clustering algorithm with elbow method. *Comput. Intell. Neurosci.* **2021**, 4553832 (2021).

**Acknowledgments**
**Funding:** This work was supported by the Strategic Priority Research Program of the Chinese Academy of Sciences (XDB0540300 to Q.B.), the National Key Research and Development Program of China (2023YFE0113300 to Q.B. and 2022YFF0707000 to C.L.), the National Natural Science Foundation of China (22327901 to M.L.) and (22574166 to Q.B.), the Science and Technology Innovation Talent and Service Special Project of Hubei Province (2023EHA003 to Q.B.), the Minerva Foundation (recipient: L.F.), the Israel Science Foundation (1874/22 to L.F.), the Rising Tide Foundation (723021 to L.F.), the Swiss Society for Cancer Prevention (P152815 to L.F.), the Israel Ministry of Health (714754 to L.F.), the European Union ERC Advanced Grant Steady NMR (101200719 to L.F.), and the Perlman Family Foundation (recipient: L.F.). **Author contributions:** X.L.: Writing—original draft, conceptualization, investigation, writing—review and editing, methodology, data curation, validation, formal analysis, software, and visualization. Sufei Wang: Writing—original draft and writing—review and editing. J.Z.: Data curation, validation, and formal analysis. ShaSha Wang: Resources and data curation. P.S.: Conceptualization, writing—review and editing, data curation, validation, and formal analysis. X.Z.: Conceptualization, writing—review and editing, methodology, data curation, validation, supervision, formal analysis, software, and visualization. M.L.: Conceptualization, investigation, writing—review and editing, resources, funding acquisition, validation, supervision, project administration, and visualization. C.L.: Writing—review and editing, funding acquisition, and supervision. L.F.: Writing—original draft, conceptualization, writing—review and editing, resources, and funding acquisition. Q.B.: Writing—original draft, conceptualization, investigation, writing—review and editing, methodology, resources, funding acquisition, data curation, validation, supervision, formal analysis, software, project administration, and visualization. **Competing interests:** The authors declare that they have no competing interests. **Data, code, and materials availability:** All data and code needed to evaluate and reproduce the results in the paper are present in the paper and/or the Supplementary Materials. The raw data underlying all figure panels have been deposited in the Zenodo Digital Repository, available at https://doi.org/10.5281/zenodo.20482155. This study did not generate new materials.

Submitted 17 January 2026
Accepted 9 July 2026
Published 21 August 2026
10.1126/sciadv.aef4377

ScienceAdvances

# High–spatiotemporal resolution deuterium metabolic imaging enables in vivo phenotyping of intra- and intertumoral heterogeneity

Xinjie Liu, Sufei Wang, Jinrui Zhao, ShaSha Wang, Peng Sun, Xin Zhou, Maili Liu, Chaoyang Liu, Lucio Frydman, and Qingjia Bao

*Sci. Adv.* **12** (34), eaef4377. DOI: 10.1126/sciadv.aef4377